



HAL
open science

Numerical investigation of the relative effect of disc bulging and ligamentum flavum hypertrophy on the mechanism of central cord syndrome

Nicolas Bailly, Lucien Diotalevi, Marie-Hélène Beausejour, Eric Warnac,
Jean-Marc Mac-Thiong, Yvan Petit

► To cite this version:

Nicolas Bailly, Lucien Diotalevi, Marie-Hélène Beausejour, Eric Warnac, Jean-Marc Mac-Thiong, et al.. Numerical investigation of the relative effect of disc bulging and ligamentum flavum hypertrophy on the mechanism of central cord syndrome. *Clinical Biomechanics*, 2020, 74, pp.58-65. 10.1016/j.clinbiomech.2020.02.008 . hal-03226854

HAL Id: hal-03226854

<https://amu.hal.science/hal-03226854>

Submitted on 15 May 2021

HAL is a multi-disciplinary open access archive for the deposit and dissemination of scientific research documents, whether they are published or not. The documents may come from teaching and research institutions in France or abroad, or from public or private research centers.

L'archive ouverte pluridisciplinaire **HAL**, est destinée au dépôt et à la diffusion de documents scientifiques de niveau recherche, publiés ou non, émanant des établissements d'enseignement et de recherche français ou étrangers, des laboratoires publics ou privés.

44 **Abstract**

45 *Background:* The pathogenesis of the central cord syndrome is still unclear. While there is a
46 consensus on hyperextension as the main traumatic mechanism leading to this condition, there
47 is yet to be consensus in studies regarding the pathological features of the spine (intervertebral
48 disc bulging or ligamentum flavum hypertrophy) that could contribute to clinical manifestations.

49 *Methods:* A comprehensive finite element model of the cervical spine segment and spinal cord
50 was used to simulate high-speed hyperextension. Four stenotic cases were modelled to study
51 the effect of ligamentum flavum hypertrophy and intervertebral disc bulging on the von Mises
52 stress and strain.

53 *Findings:* During hyperextension, the downward displacement of the ligamentum flavum and a
54 reduction of the spinal canal diameter (up to 17%) led to a dynamic compression of the cord.
55 Ligamentum flavum hypertrophy was associated with stress and strain (peak of 0.011 Mpa and
56 0.24, respectively) in the lateral corticospinal tracts, which is consistent with the histologic
57 pattern of the central cord syndrome. Linear intervertebral disc bulging alone led to a higher
58 stress in the anterior and posterior funiculi (peak 0.029 Mpa). Combined with hypertrophic
59 ligamentum flavum, it further increased the stress and strain in the corticospinal tracts and in
60 the posterior horn (peak of 0.023 Mpa and 0.35, respectively).

61 *Interpretation:* The stenotic typology and geometry greatly influence stress and strain
62 distribution resulting from hyperextension. Ligamentum flavum hypertrophy is a main feature
63 leading to central cord syndrome.

64 **Keywords**

65 Central cord syndrome, hyperextension, cervical spine, spinal cord, spondylosis

66

67

68

69 **1. Introduction**

70 Central cord syndrome (CCS) is the most common type of incomplete traumatic cervical spinal
71 cord injury and its incidence is increasing in older patients (McKinley et al., 2007; Thompson et
72 al., 2015). This syndrome is characterized by a greater motor impairment in the upper limbs
73 than in the lower limbs. It was first described in 1954 by Schneider et al. (Schneider et al., 1954),
74 and was attributed to hemorrhage damages and swelling, predominantly in the spinal grey
75 matter and in the lateral corticospinal tracts. Later, MRI and histopathological studies
76 substantiated this, showing a predominance of axonal injury in the lateral column (Collignon et
77 al., 2002; Jimenez et al., 2000; Martin et al., 1992; Quencer et al., 1992).

78 The pathogenesis of CCS was initially described as a compression of the spinal cord during
79 hyperextension of the neck, usually combined with stenosis of the cervical spinal canal (Molliqaj
80 et al., 2014; Schneider et al., 1954). However, the main stenotic features of the spine
81 contributing to CCS are still debated: the spinal cord is either compressed posteriorly from
82 anterior bulging of the ligamentum flavum (Schneider et al., 1954), anteriorly from marginal
83 osteophytes, anteriorly from disc bulging (Dai et al. 2000), or by any combination of those three
84 features. Histological and MRI studies suggested that axonal injury was mainly located in the
85 lateral columns (Collignon et al., 2002; Jimenez et al., 2000; Martin et al., 1992; Quencer et al.,
86 1992), which may then be the location of maximal stresses in the spinal cord in the presence of
87 CCS. Unfortunately, histological studies only present indirect evidence from a posteriori
88 evaluations, with little understanding of the mechanism of injury.

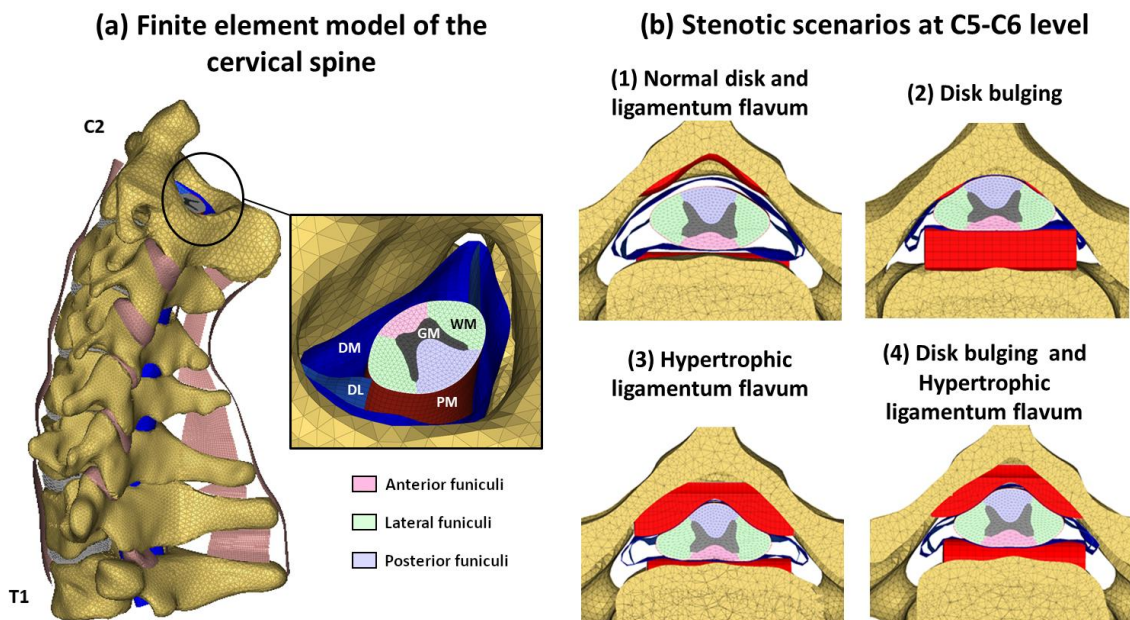
89 The latest advances in finite element (FE) analysis enable the replication of such injury
90 mechanisms and the estimation of the strain and stress distribution in the spinal cord
91 throughout traumatic events. Li et al. (2010) simulated the extension, flexion and compression
92 of the cervical spinal cord submitted to an anterior or posterior compressive force. Nishida et al.
93 (2012) simulated extension with the cervical spinal cord submitted to posterior compression
94 from a simplified hypertrophic ligamentum flavum model. These studies showcased peak
95 stresses located in the grey matter and both anterior and posterior funiculi, as opposed to
96 histopathological studies reporting the predominance of axonal injury in the lateral column
97 (Martin et al., 1992; Quencer et al., 1992). Therefore, the exact pathogenesis of traumatic
98 central cord syndrome remains largely debated, although it affects an increasing number of
99 patients (Thompson et al., 2015).

100 The goal of this paper is to investigate the injury mechanisms of traumatic CCS. Using a
101 comprehensive cervical FE model, this study will specifically assess the relative contributions of
102 intervertebral disc bulging and ligamentum flavum hypertrophy on the stress and strain
103 distributions within the spinal cord during an hyperextension of the neck.

104 2. Methods

105 2.1. Finite element modelling of the cervical spine

106 A finite element (FE) model of the cervical spine (C2-T1) described in previous works
107 (Beauséjour et al., 2019; Fradet et al., 2014; Taso et al., 2015) was adapted for this study. This
108 model of a 50th percentile adult male subject includes vertebrae, intervertebral discs, as well as
109 six spinal ligaments: anterior and posterior longitudinal ligaments, zygapophyseal joint
110 ligaments, ligamentum flavum, interspinous ligaments and nuchal ligament (Fig. 1(a)).



111

112 **Fig. 1. (a) Finite element model of the cervical spine and (b) Stenotic scenario at C5-C6 levels in**
113 **the 4 tested cases. Abbreviation: DM, dura mater; PM, pia mater; DL, denticulate ligament;**
114 **WM, white matter; GM, grey matter.**

115 Each vertebra was defined as a rigid body. Material laws for the ligaments were defined by
116 tabulated, non-linear, strain-rate dependent, stress-strain curves derived from mean force-
117 deflection curves measured in experimental studies (Mattucci et al., 2012; Mattucci and Cronin,
118 2015). The interspinous ligament force-deflection curve was applied to the adjacent nuchal

119 ligament, as this ligament was not included in the experimental studies. Toe regions of the
 120 curves were calibrated in a previous study to account for the initial elongation of cervical
 121 ligaments (Beauséjour et al., 2019). The intervertebral discs were divided into a nucleus
 122 pulposus (20% of the disk volume) and an annulus fibrosus ground substance. They were then
 123 associated with first-order Mooney-Rivlin hyper-elastic material laws. The annulus fibrosus was
 124 divided into three sections (anterior, posterior and lateral) reinforced with specific tension-only
 125 spring elements organized in concentric lamellae with a crosswise pattern at $\pm 35^\circ$ to represent
 126 the collagen fibers (Wagnac et al., 2011). The initial material properties of the discs were initially
 127 defined from Schmidt et al. (2006) and Shirazi-adl et al. (1986), and then modified and calibrated
 128 for dynamic flexion and extension, as described in section 2.2.

129 The FE model also includes a spinal cord model previously described by Fradet et al. (2014), Taso
 130 et al. (2015) and Diotalevi et al. (2020). It is composed of white and grey matter, denticulate
 131 ligaments, pia mater and dura mater (Fig. 1 (a)). Meshing was performed with pentahedral (6
 132 nodes) 3D elements for the white and grey matter, and quadratic (4 nodes) shell elements for
 133 the ligaments, the pia and the dura mater. The proximal end of the spinal cord was attached to
 134 the C2 vertebra to simulate the connection with the brain stem and to guide the spinal cord
 135 movement. The rest of the spinal cord was left unrestrained. Material laws and properties of the
 136 FE model are summarized in Table 1.

137

138 Table 1: Finite element model material properties

	Type of elements	Material law	Material parameters (units: g, mm, ms)	References
Spinal cord:				
Grey matter	Pentahedral Brick	Stress–strain tabulated	Curves in Fradet et al. 2016	(Fradet et al., 2016)
White matter	Pentahedral Brick	Stress–strain tabulated	Curves in Fradet et al. 2016	(Fradet et al., 2016)
Pia mater	Quad	Linear elastic	$\rho = 0.001$; $\nu = 0.45$; $E = 2.3$	(Fradet et al., 2016)
Dura mater	Quad	Linear elastic	$\rho = 0.001$; $\nu = 0.45$; $E = 5$	(Fradet et al., 2016)
Dentate ligament	Quad	Linear elastic	$\rho = 0.001$; $\nu = 0.45$; $E = 10$	(Fradet et al., 2016)
Ligaments:				
	Quad Except capsular ligament (tria)	Stress-strain nonlinear curves	Curves derived from Mattucci and Cronin 2015	(Mattucci and Cronin, 2015)

139 2.2. Dynamic calibration of the discs

140 The dynamic calibration of the model was performed by adjusting the material properties of the
141 annulus extracellular matrix and nucleus until the moment-rotation curves of each functional
142 spinal unit (C2-C3 to C7-T1) fit with experimental results from Barker et al. (2014). For each
143 spinal unit, the lower vertebra was fixed, while a rotation of 500 deg.s⁻¹ in flexion and extension
144 was applied to the upper vertebra. The axis of rotation of each unit was determined as
145 described in Amevo et al. (1991) to replicate the experimental conditions of Barker et al. (2014).
146 Since the C7-T1 axis was not included in this study, the data for C6-C7 was used to set the axis of
147 rotation.

148 To determine the goodness of fit between simulation and experimental results, three criteria
149 were used: corridor rating, shape rating and size rating. For each data point, the corridor rating
150 was set to 1 if the simulation results fit inside one standard deviation, and to 0 if the result was
151 outside two standard deviations. For results between one and two standard deviations, a linear
152 relation between 0 (outside 2 standard deviations) and 1 (equal to one standard deviation) was
153 calculated. The final corridor rating value was obtained by averaging corridor rating values at
154 every data point. The size rating and shape rating were measured as defined in Barker et al.
155 (2017). The size rating (equation (1)) is the ratio between the area below the simulation curve
156 $y(t)$ and the experimental curve $x(t)$. The larger value is set as the denominator.

$$157 \quad \text{Size rating} = \frac{\sum_{i=1}^n y^2(t_{min} + i * \Delta t)}{\sum_{i=1}^n x^2(t_{min} + (m+i) * \Delta t)} \quad (1)$$

158 The shape rating (equation (2)) compares the slope and the change in the slope of the simulated
159 curve $y(t)$ against the experimental curve $x(t)$. The phase-shifting m , representing the x-intercept
160 shifting, was not enabled for the measure of the shape rating. Therefore, m was set to 0.

$$161 \quad \text{Shape rating} = \frac{\sum_{i=0}^{n-1} x(t_{min} + (m+i) * \Delta t) * y(t_{min} + i * \Delta t)}{\sqrt{\sum_{i=0}^{n-1} x^2(t_{min} + (m+i) * \Delta t) * \sum_{i=0}^{n-1} y^2(t_{min} + i * \Delta t)}} \quad (2)$$

162 An average of these three criteria was calculated for the moment-rotation curves in flexion and
163 extension, and an overall rating was measured as the average between the rate in flexion and
164 extension. It was chosen to target a rating of between 0.65 and 1, based on a rating scale
165 defined by Cesari et al. (2001).

166 Calibration of the disk material properties was performed by adjusting the parameters C_{10} and
167 C_{01} of the Mooney-Rivlin hyper-elastic material laws used for the annulus and nucleus for each
168 spinal unit. First, the dynamic flexion and extension of each unit were performed with the quasi-
169 static material properties of the disk (Schmidt et al., 2006). If the ratings met our criteria, no
170 calibration was performed. Otherwise, a scaling factor of 0.5 to 15 was applied to the annulus
171 and nucleus rigidity (parameters C_{10} and C_{01} of the material law), while maintaining the C_{10} to C_{01}
172 ratio. The range of 0.5 to 15 was chosen to vary the properties grossly between values
173 determined in other studies for the lumbar disk in quasi-static (Schmidt et al., 2006) and
174 dynamic (Wagnac et al., 2012) loadings. A C_{10} -to- C_{01} ratio was maintained based on the results
175 of a preliminary sensitivity study, which showed that this ratio had no significant impact on the
176 FSU mobility. If no satisfying result was obtained, the rigidity of the nucleus and the anterior,
177 lateral and posterior bulk annuli were independently iteratively scaled until the best overall
178 rating (extension and flexion) was obtained.

179 **2.3. Finite element modelling of the spondylotic stenosis**

180 The original geometry of the vertebral canal was modified from C4 to C7 to simulate a stenotic
181 canal area. First, the canal diameter was reduced by 3 mm, corresponding to the average
182 reduction seen in patients with spondylosis (Shedid and Benzel, 2007). Two spondylotic features
183 were also included: linear disc bulging and hypertrophic ligamentum flavum. Four cases were
184 modelled, based on the presence or absence of these two features (Fig. 1 (b)).

185 As canal stenosis associated with cervical spondylosis typically occurs at several levels, these
186 features were inserted at three intervertebral levels: C4-C5, C5-C6 and C6-C7 (displayed in red in
187 Fig. 3) (Stevenson et al., 2016). Hypertrophic ligamentum flavum and linear disc bulging
188 idealized geometries (Fig. 1 (b)) were defined based on MRI measurements of typical cases
189 found in our institution database (Thompson et al., 2015), and were consistent with the
190 literature (Muhle et al., 1998; Song et al., 2006; Tani et al., 1999; Yu et al., 1983). Idealization of
191 these features is also in accordance with the literature (Kim et al., 2013). These features were
192 meshed with hexahedral (8 nodes) 3D elements and defined as rigid bodies.

193 Modelling of the ligamentum flavum hypertrophy and disc bulging was performed in a
194 preliminary simulation, with the neck placed in an upright position, and a normal C2-C7 lordosis
195 angle of 22.7° according to Gore et al. (1986). The spondylotic features were moved alongside

196 the anteroposterior axis into the canal at the three affected levels to compress the cord and
197 reach 40% reduction of the sagittal canal diameter, which corresponds to a typical degree of
198 compression in cervical spondylosis, according to Ogino et al. (1983). Then, the disk bulging
199 features were fixed to the lower vertebra while the hypertrophic ligamentum flavum features
200 were fixed to the upper vertebra of each segment. These altered geometries were then used in
201 the neck hyperextension simulation. Both spondylotic features had frictionless contacts with the
202 dura mater.

203 **2.4. Loading and boundary conditions**

204 Hyperextension was achieved by fixing T1 in space and applying 60 degrees of rotation in the
205 median plane to C2 at 500 deg.s^{-1} , around a mobile axis located at the center of the vertebral
206 foramen of C2. This rotational speed of 500 deg.s^{-1} has been observed during typical car crash
207 scenarios (Panzer et al., 2011) and a 60° magnitude of rotation approximates the maximal
208 amplitude, without soft-tissue injury, as reported by Barker et al. (2014).

209

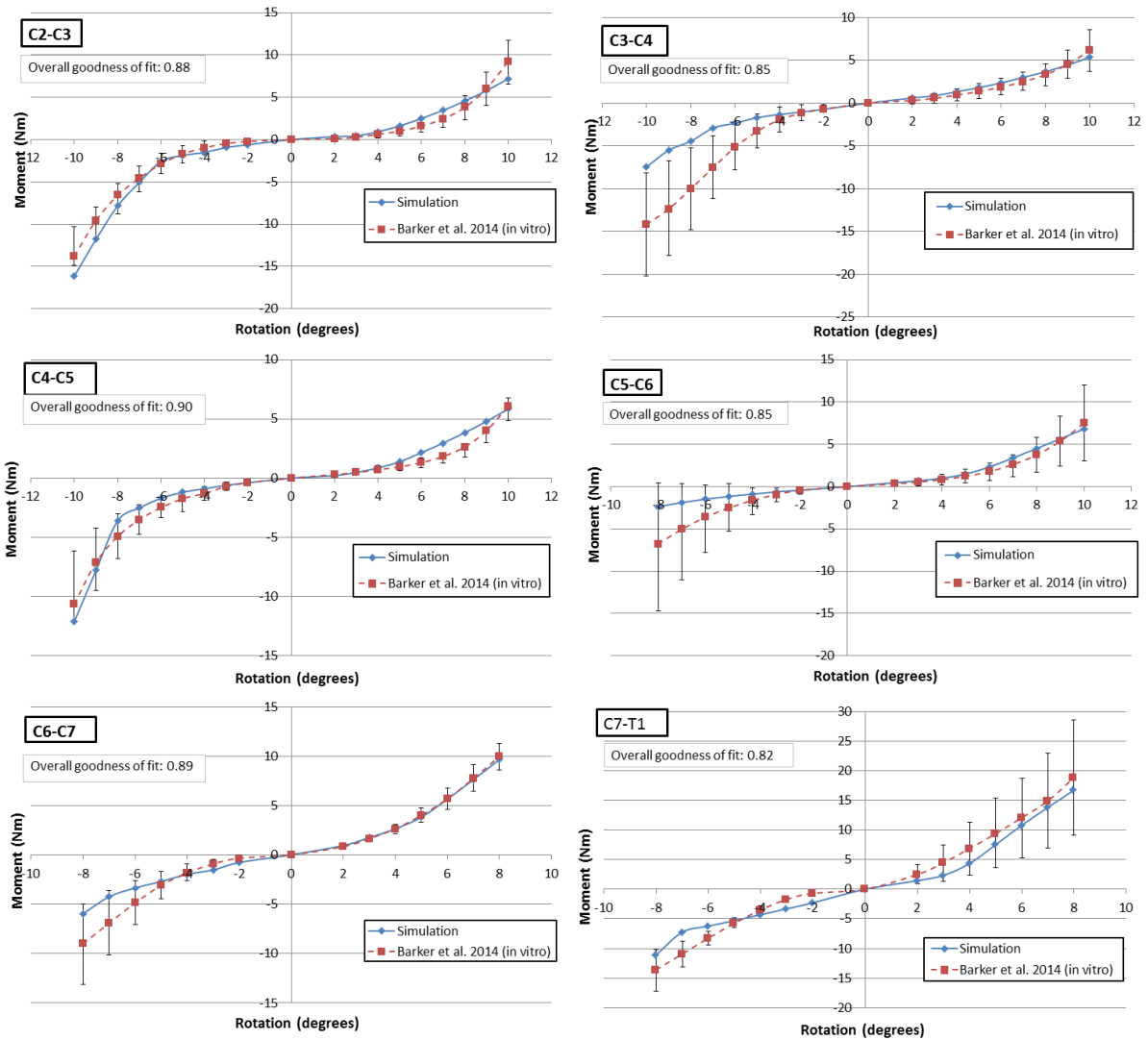
210 **2.5 Analysis**

211 Model outcomes were von Mises strains and stresses in the grey and white matter. Both
212 outcomes were extracted at every node of the FE model. A simple averaging of their values was
213 performed by summing the studied tensor equivalent invariant measured at the finite element
214 corner adjacent to the studied node, and then dividing them by the number of finite element
215 corners adjacent to this node. This method was used to avoid mathematical aberrations on the
216 results.

217 **3. Results**

218 **3.1. Dynamic calibration**

219 Goodness of fit scores between the model's FSU kinematics and experimental results from
220 Barker et al. (2014) varied from 0.82 to 0.90 (Fig. 2). The resulting C_{01} and C_{10} parameters for
221 the annulus and nucleus are presented in Appendix 1. The moment-rotation curves generally lie
222 within one standard deviation of the experimental results (overall corridor ratings between 0.76
223 and 1) (Fig. 2).

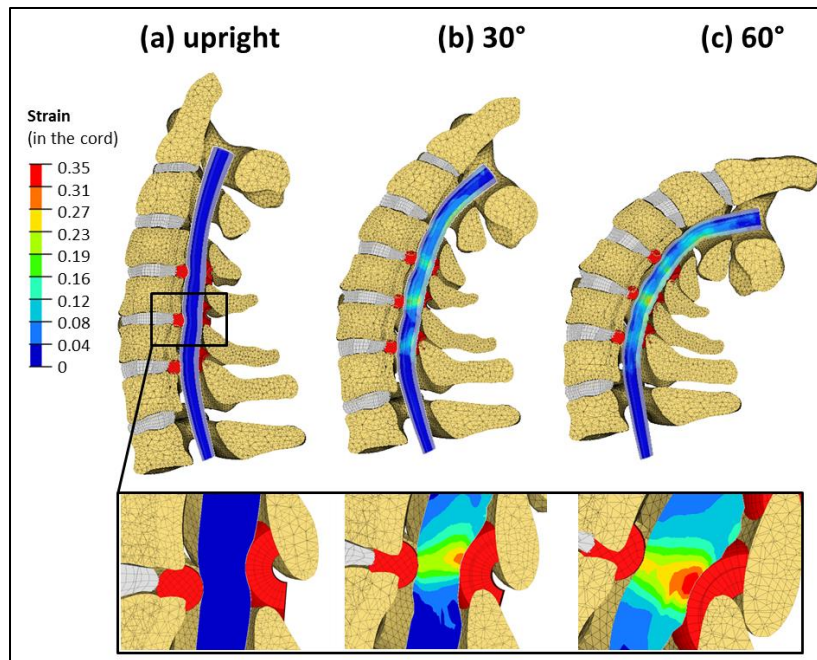


224
225

Fig. 2: Cervical FSU moment-rotation diagrams at rotational velocity of 500 deg.s⁻¹

226 **3.2. 2. Stress and strain distribution during hyperextension**

227 Figure 3 presents a sagittal cross-section of the cervical spine during hyperextension and the
 228 strain distribution in the cord. During hyperextension, the rotation of the upper adjacent
 229 vertebra induced a downward displacement of the ligamentum flavum: at the C5-C6 level, the
 230 ligamentum flavum, initially located above the disk, ended up below it at the end of
 231 hyperextension (Fig. 3). This was associated with a reduction of the minimal spinal canal antero-
 232 posterior diameter (up to 17% decrease at C5-C6). The location of this canal reduction also
 233 shifted downward during the hyperextension: it is above the disk at 30°, but below the disc at
 234 60° of extension. The highest stress and strain were observed at C5-C6 (Fig. 3).



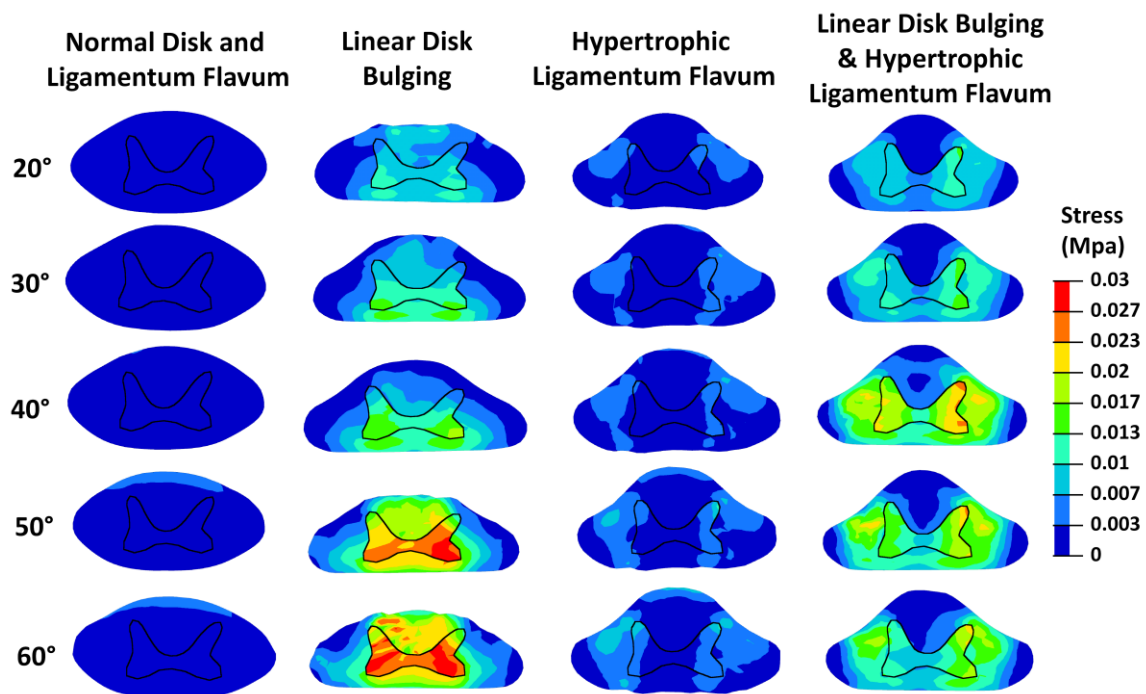
235

236 **Fig. 3. Strain distribution in a sagittal cross-section of the spinal cord during hyperextension**
 237 **with a stenotic case presenting a narrowed canal, hypertrophic ligamentum flavum and linear**
 238 **disk bulging (both displayed in red)**

239 In the transverse plane, stress and strain at C5-C6 increased gradually throughout extension,
 240 with different patterns depending on the stenotic cases (Fig. 4 and 5). We observed that the
 241 stress distribution did not exactly match the strain distribution due to the higher rigidity of the
 242 grey matter compared to white matter. In the normal column (reference case), the peak stress
 243 and strain were located in the posterior funiculi, and were respectively equal to 0.0017 kPa and
 244 0.08 at 30° of extension, and 0.0045 kPa and 0.17 at 60° (Fig. 4 and 5). In the presence of linear
 245 disk bulging alone, stress and strain were initiated in the anterior and posterior funiculi and
 246 increased gradually in both areas. At 30° extension, the peak stress and strain were respectively
 247 9 and 4.2 times higher than in the normal column (respectively 6.5 and 3.2 times higher at 60°).
 248 The peak stress was observed in the anterior horn while the peak strain was located in the
 249 anterior and posterior funiculi. In the presence of hypertrophic ligament flavum alone, the peak
 250 stress and strain first appeared in the posterior and medial parts of the lateral funiculi, where
 251 they increased gradually, as well as in the posterior horn. At 30°, the peak stress and strain were
 252 respectively 4.1 and 2.62 times greater than in the normal column (respectively 2.5 and 1.5
 253 times higher at 60°). In the presence of both linear disk bulging and hypertrophic ligament

254 flavum, stress and strain initiated in both the posterior and medial parts of the lateral funiculi
 255 and in the anterior funiculi. At 30° extension, the peak stress and strain were mainly located in
 256 the posterior and medial parts of the lateral funiculi and in the posterior horn, and were
 257 respectively 9.4 and 3.8 times higher than in the normal column (respectively 5.2 and 2.1 times
 258 higher at 60°) (Fig. 4 and 5).

259 In every simulation, the presence of a hypertrophic ligamentum flavum was associated with high
 260 stresses and strains in the medial part of the lateral funiculi at the early stage of the extension,
 261 which corresponds to the main damaged region in CCS (Martin et al., 1992; Quencer et al., 1992)
 262 and to the location of the corticospinal tract. The addition of a linear disk bulging into the canal
 263 in the presence of hypertrophic ligamentum flavum increased the overall level of stress in these
 264 areas during extension.

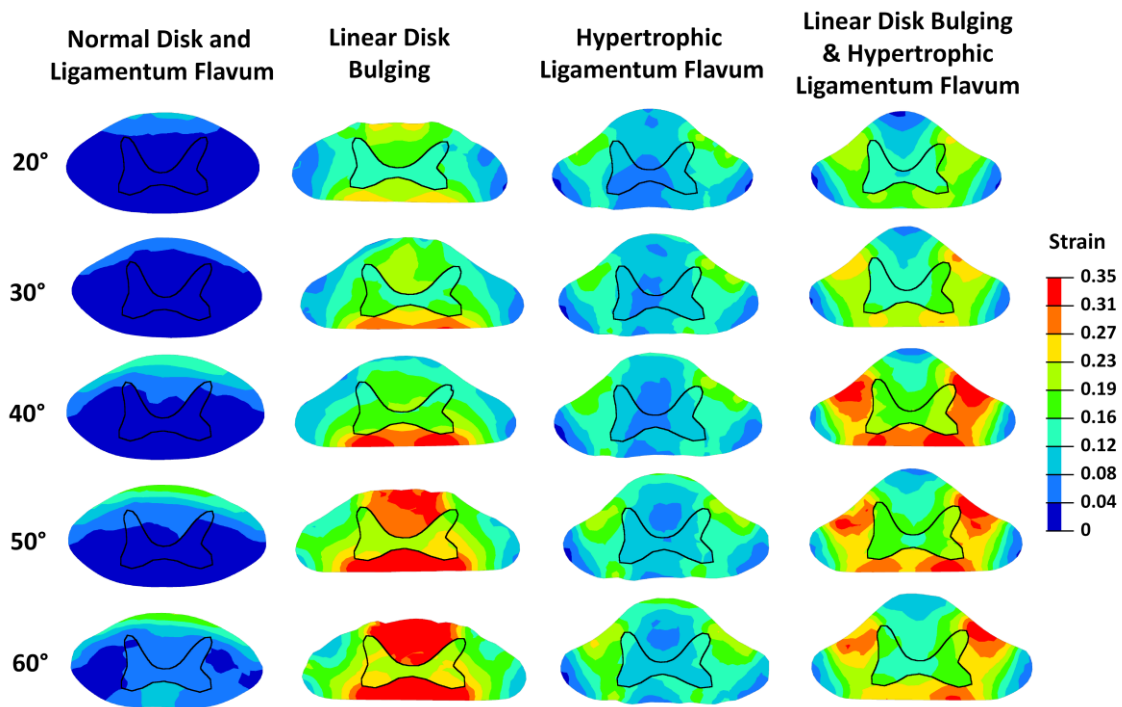


265

266

267 **Fig. 4. Stress distributions in a transversal cross-section of the spinal cord at the C5-C6**
 268 **intervertebral level at 5 extension angles for the 3 different stenotic cases**

269



270

271 **Fig. 5. Strain distributions in a transversal cross-section of the spinal cord at the C5-C6**
 272 **intervertebral level at 5 extension angles for 3 different stenotic cases.**

273

274 **4. Discussion**

275 This FE method study is the first to investigate the spinal cord dynamics with different cases of
 276 cervical canal stenosis leading to CCS. The results demonstrate that the geometry and position
 277 of the stenotic feature greatly influence the stress and strain distributions throughout the
 278 hyperextension movement of the neck. In particular, the presence of hypertrophic ligamentum
 279 flavum induced specific stress and strain distributions that are consistent with histologic findings
 280 related to CCS (Jimenez et al., 2000; Martin et al., 1992; Quencer et al., 1992). This provides
 281 important insights into the pathophysiology of CCS.

282 The mechanism of CCS is described as a transverse compression of the spinal cord, during an
 283 hyperextension of the neck, due to a reduction of the cervical spinal canal size induced by the
 284 bulging of the ligamentum flavum (Schneider et al., 1954). A reduction of the canal diameter
 285 was indeed observed by Muhle et al. (1998) in some spondylotic patients performing a neck
 286 extension in a kinematic MRI. In the present study, up to a 17% canal reduction was observed at

287 the C5-C6 intervertebral level, but this was also associated with a downward displacement of
288 the ligamentum flavum (Fig. 3). This combined phenomenon modifies the pinching zone of the
289 cord: it was above the disc in the neutral position, but below the disc at 60° of extension. This
290 might explain the significant strain increase in the cord (>25% at 60° of extension) despite the
291 small reduction in the canal diameter (6% at 60° of extension).

292 In the presence of the hypertrophic ligamentum flavum, the peak stress and strain were
293 observed in the posterior and medial parts of the lateral funiculi, close to the posterior horn of
294 the grey matter. This area matches those where most of the axonal damage and Wallerian
295 degeneration are found in histological studies of CCS (Jimenez et al., 2000; Martin et al., 1992;
296 Quencer et al., 1992). Conversely, stress patterns with linear disk bulging alone were mostly
297 distributed in the anterior and posterior funiculi. These results suggest that the presence of
298 hypertrophic ligament flavum is an important factor in the pathogenesis of CCS, as proposed by
299 Schneider et al. (1954) and discussed by many others (Dai and Jia, 2000; Li and Dai, 2010;
300 Quencer et al., 1992). The concomitant presence of hypertrophic ligamentum flavum and linear
301 disk bulging further increases the stresses and strains in the lateral funiculi by inducing an
302 additional pincer effect from combined anterior and posterior compression of the spinal cord
303 during extension, as suggested by previous authors (Morishita et al., 2013; Nishida et al., 2012).

304 The differences in stress and strain distributions induced by hypertrophic ligamentum flavum
305 and disk bulging may be explained by their geometry and their location of contact with the cord.
306 In the present study, disk bulging applies a linear compression to the anterior part of the cord,
307 resulting in strain concentrations at the contact area decreasing toward the center of the cord.
308 Conversely, the hypertrophic ligamentum flavum applies two lateral contact forces converging
309 toward the center of the spinal cord, forming a pincer movement between contralateral
310 segments of the ligamentum flavum. This induces centralized stresses and strains in the cord. In
311 previous FE method studies, Nishida et al. (2012) used other simplified geometries to model the
312 pinching force applied to the cord during hyperextension: the ligamentum flavum was modelled
313 with a linear shape, and three types of anterior compression were used (central, lateral or
314 diffuse type). Each of these configurations also presented a unique stress pattern, mainly
315 located in the grey matter and in the anterior and posterior funiculi. However, none led to high
316 levels of stress in the corticospinal tracts, as observed in the present study. This confirms that
317 different stenotic configurations lead to different stress and strain distributions, which is

318 consistent with the great variability of syndromes and outcomes associated with hyperextension
319 injuries without instabilities (McKinley et al., 2007). Future FE method studies may need to
320 consider patient-specific model geometry to understand their unique injury mechanism.

321 The area of highest stress and strain concentrations generally observed in the presence of
322 hypertrophic ligamentum flavum is located in the lateral corticospinal tract, which is associated
323 with motor control, and is strongly linked with hand dexterity (Courtine et al., 2007). According
324 to Foerster (1936) and Schneider et al. (1958), the lateral corticospinal tracts have a
325 somatotopic arrangement in which the medial part is associated with upper extremity function,
326 while the lateral part is associated with lower extremity function. Based on this somatotopy,
327 greater motor impairment in the upper limbs observed in CCS would be explained by higher
328 damage in the medial part of the corticospinal tract than in the lateral part. However, this
329 hypothesis has been challenged by histologic findings showing uniform damage to the lateral
330 corticospinal tract (Quencer et al. 1992) and by Nathan and Smith (1955), who demonstrate that
331 the lateral tracts are not laminated into functional units, but rather, that the motor fiber
332 involved in upper and lower limb function were interlaced. This hypothesis was reinforced by
333 several studies on monkeys showing that sectioning of the entire corticospinal tract lead to
334 greater dysfunction in the upper limbs than in the lower limbs (Bucy et al., 1966; Nathan and
335 Smith, 1955). The results of the present study are compatible with a CCS in the two theories. On
336 the one hand, in the presence of the ligamentum flavum, high stresses were mostly distributed
337 in the corticospinal tracts, suggesting that the entire lateral corticospinal tract was affected
338 (Quencer et al. 1992; Jimenez, Marcillo, and Levi 2000). On the other hand, peak stress in the
339 white matter was mainly seen in the medial part of the lateral funiculi, next to the posterior
340 horn, which is the zone associated with upper extremity function in the somatotopic
341 arrangement described by Foerster (1936). To further correlate the stress pattern in the cord
342 with neurological damage and discriminate these two theories, future FE method studies should
343 consider reproducing patient-specific geometry and injury dynamics and compare them with
344 clinical observations.

345 This study presents some limitations associated with assumptions and simplifications. First, the
346 cerebro-spinal fluid was not included because it was absent in the stenotic zone of most cases of
347 CCS with severe spinal stenosis found in our institutional database (Thompson et al., 2015).
348 Secondly, disks and ligament behaviour in the current model were calibrated based on data

349 from non-pathological spine segments (Barker et al., 2014), but a stenotic spine is expected to
350 be more rigid and less likely to sustain a 60° hyperextension. However, this does not challenge
351 our conclusions since high stress and strain appeared at less than 30° of extension, which is a
352 normal range of extension for the elderly, according to Muhle et al. (1998). Thirdly, the
353 mechanical behaviour of white and grey matter was defined by isotropic strain rate-dependent
354 tabulated laws derived from experiments reported in the literature (Fradet et al., 2016).
355 Nevertheless, these materials are possibly anisotropic as they are notably composed of
356 neurones, myelin, glial cells, etc. In order to further study the local stress concentrations and the
357 affected axonal tracts, future studies should be performed to supplement the understanding
358 and characterization of the local behaviour of the spinal cord white and grey matter and to
359 refine finite element models. Finally, no direct link could be established between the results of
360 this study and neurological injury because no accepted stress and strain thresholds have been
361 defined for neurological injury of the spinal cord and because the model was not associated with
362 the specific geometry and injury dynamic of a patient with identified neurological evaluation.
363 Future work should focus on reproducing patient-specific injuries and establishing a neurological
364 injury threshold.

365

366 **5. Conclusions**

367 This study is the first, to the authors' knowledge, to examine the dynamics of a detailed
368 osteoligamentous spine and spinal cord model for a typical traumatic event associated with
369 central cord syndrome. The hypothesis suggesting a pinching of the spinal cord by hypertrophic
370 ligament flavum and linear disk bulging during a hyperextension was investigated in this study. It
371 was found that only ligamentum flavum hypertrophy was associated with high stress and strain
372 in the corticospinal tracts, which is consistent with the histologic pattern of the central cord
373 syndrome. The presence of a linear disk bulging alone was not associated with such a pattern,
374 but when combined with hypertrophic ligament flavum, increased the overall level of stress and
375 strain in the corticospinal tract.

376

377

378 **6. References**

- 379 Amevo, B., Worth, D., Bogduk, N., 1991. Instantaneous axes of rotation of the typical cervical
380 motion segments: a study in normal volunteers. *Clin. Biomech.* 6, 111–117.
- 381 Barker, J.B., Cronin, D.S., Chandrashekar, N., 2014. High Rotation Rate Behavior of Cervical Spine
382 Segments in Flexion and Extension. *J. Biomech. Eng.* 136, 121004-121004–10.
383 <https://doi.org/10.1115/1.4028107>
- 384 Barker, J.B., Cronin, D.S., Nightingale, R.W., 2017. Lower cervical spine motion segment
385 computational model validation: Kinematic and kinetic response for quasi-static and
386 dynamic loading. *J. Biomech. Eng.* 139, 061009.
- 387 Beauséjour, M.-H., Petit, Y., Arnoux, P.J., Wagnac, E., 2019. Comparison of two intervertebral
388 disc failure models in a numerical C4-C5 trauma model. Presented at the 41st
389 Engineering in Medicine and Biology Conference., Berlin.
- 390 Bucy, P.C., Ladpli, R., Ehrlich, A., 1966. Destruction of the Pyramidal Tract in the Monkey: The
391 Effects of Bilateral Section of the Cerebral Peduncles. *J. Neurosurg.* 25, 1–23.
392 <https://doi.org/10.3171/jns.1966.25.1.0001>
- 393 Cesari, D., Compigne, S., Scherer, R., Xu, L., Takahashi, N., Page, M., Asakawa, K., Kostyniuk, G.,
394 Hautmann, E., Bortenschlager, K., 2001. WorldSID prototype dummy biomechanical
395 responses. SAE Technical Paper.
- 396 Collignon, F., Martin, D., Lénelle, J., Stevenaert, A., 2002. Acute traumatic central cord
397 syndrome: magnetic resonance imaging and clinical observations. *J. Neurosurg. Spine*
398 96, 29–33.
- 399 Courtine, G., Bunge, M.B., Fawcett, J.W., Grossman, R.G., Kaas, J.H., Lemon, R., Maier, I., Martin,
400 J., Nudo, R.J., Ramon-Cueto, A., Rouiller, E.M., Schnell, L., Wannier, T., Schwab, M.E.,
401 Edgerton, V.R., 2007. Can experiments in nonhuman primates expedite the translation
402 of treatments for spinal cord injury in humans? *Nat. Med.* 13, 561–566.
403 <https://doi.org/10.1038/nm1595>
- 404 Dai, L., Jia, L., 2000. Central Cord Injury Complicating Acute Cervical Disc Herniation in Trauma.
405 *Spine* 25, 331.
- 406 Diotalevi, L., Bailly, N., Wagnac, E., Mac-Thiong, J-M., Goulet, J., Petit, Y., 2020. Dynamics of
407 spinal cord compression with different patterns of thoracolumbar burst fractures:
408 Numerical simulations using finite element modelling. *Clinical Biomechanics* 72, 186-
409 194. <https://doi.org/10.1016/j.clinbiomech.2019.12.023>

410 Foerster, O., 1936. Symptomatologie der Erkrankungen des Rückenmarks und seiner Wurzeln,
411 in: Foerster, O., Gagel, O., Környey, St., Lotmar, F., Marburg, O., Stenvers, H.W. (Eds.),
412 Rückenmark Hirnstamm · Kleinhirn, Handbuch der Neurologie. Springer Berlin
413 Heidelberg, Berlin, Heidelberg, pp. 1–403. [https://doi.org/10.1007/978-3-642-50776-](https://doi.org/10.1007/978-3-642-50776-2_1)
414 [2_1](https://doi.org/10.1007/978-3-642-50776-2_1)

415 Fradet, L., Arnoux, P.J., Callot, V., 2014. Finite element study of cervical spinal dislocation with
416 spinal cord injury preliminary results. Presented at the Proceedings of SIMBIO-M,
417 Marseille, France.

418 Fradet, L., Arnoux, P.-J., Callot, V., Petit, Y., 2016. Geometrical variations in white and gray
419 matter affect the biomechanics of spinal cord injuries more than the arachnoid space.
420 Adv. Mech. Eng. 8, 1687814016664703. <https://doi.org/10.1177/1687814016664703>

421 Gore, D.R., Sepic, S.B., Gardner, G.M., 1986. Roentgenographic findings of the cervical spine in
422 asymptomatic people. Spine 11, 521–524. [https://doi.org/10.1097/00007632-](https://doi.org/10.1097/00007632-198607000-00003)
423 [198607000-00003](https://doi.org/10.1097/00007632-198607000-00003)

424 Jimenez, O., Marcillo, A., Levi, A.D.O., 2000. A histopathological analysis of the human cervical
425 spinal cord in patients with acute traumatic central cord syndrome. Spinal Cord 38, 532–
426 537. <https://doi.org/10.1038/sj.sc.3101052>

427 Kim, Y.H., Khuyagbaatar, B., Kim, K., 2013. Biomechanical effects of spinal cord compression due
428 to ossification of posterior longitudinal ligament and ligamentum flavum: a finite
429 element analysis. Medical engineering & physics 35, 1266-1271.

430 Li, X.-F., Dai, L.-Y., 2010. Acute Central Cord Syndrome: Injury Mechanisms and Stress Features.
431 Spine 35, E955. <https://doi.org/10.1097/BRS.0b013e3181c94cb8>

432 Martin, D., Schoenen, J., Lenelle, J., Reznik, M., Moonen, G., 1992. MRI-pathological correlations
433 in acute traumatic central cord syndrome: case report. Neuroradiology 34, 262–266.
434 <https://doi.org/10.1007/BF00588177>

435 Mattucci, S.F., Cronin, D.S., 2015. A method to characterize average cervical spine ligament
436 response based on raw data sets for implementation into injury biomechanics models. J.
437 Mech. Behav. Biomed. Mater. 41, 251–260.

438 Mattucci, S.F., Moulton, J.A., Chandrashekar, N., Cronin, D.S., 2012. Strain rate dependent
439 properties of younger human cervical spine ligaments. J. Mech. Behav. Biomed. Mater.
440 10, 216–226.

441 McKinley, W., Santos, K., Meade, M., Brooke, K., 2007. Incidence and Outcomes of Spinal Cord
442 Injury Clinical Syndromes. *J. Spinal Cord Med.* 30, 215–224.

443 Molliqaj, G., Payer, M., Schaller, K., Tessitore, E., 2014. Acute traumatic central cord syndrome:
444 A comprehensive review. *Neurochirurgie* 60, 5–11.
445 <https://doi.org/10.1016/j.neuchi.2013.12.002>

446 Morishita, Y., Maeda, T., Naito, M., Ueta, T., Shiba, K., 2013. The pincers effect on cervical spinal
447 cord in the development of traumatic cervical spinal cord injury without major fracture
448 or dislocation. *Spinal Cord* 51, 331–333. <https://doi.org/10.1038/sc.2012.157>

449 Muhle, C., Metzner, J., Weinert, D., Falliner, A., Brinkmann, G., Mehdorn, M.H., Heller, M.,
450 Resnick, D., 1998. Classification system based on kinematic MR imaging in cervical
451 spondylitic myelopathy. *Am. J. Neuroradiol.* 19, 1763–1771.

452 Nathan, P.W., Smith, M.C., 1955. LONG DESCENDING TRACTS IN MANI. REVIEW OF PRESENT
453 KNOWLEDGE. *Brain* 78, 248–303. <https://doi.org/10.1093/brain/78.2.248>

454 Nishida, N., Kato, Y., Imajo, Y., Kawano, S., Taguchi, T., 2012. Biomechanical analysis of cervical
455 spondylotic myelopathy: The influence of dynamic factors and morphometry of the
456 spinal cord. *J. Spinal Cord Med.* 35, 256–261.
457 <https://doi.org/10.1179/2045772312Y.0000000024>

458 Ogino, H., Tada, K., Okada, K., Yonenobu, K., Yamamoto, T., Ono, K., Namiki, H., 1983. Canal
459 diameter, anteroposterior compression ratio, and spondylotic myelopathy of the
460 cervical spine. *Spine* 8, 1–15.

461 Panzer, M.B., Fice, J.B., Cronin, D.S., 2011. Cervical spine response in frontal crash. *Med. Eng.*
462 *Phys.* 33, 1147–1159. <https://doi.org/10.1016/j.medengphy.2011.05.004>

463 Quencer, R.M., Bunge, R.P., Egnor, M., Green, B.A., Puckett, W., Naidich, T.P., Post, M.J.D.,
464 Norenberg, M., 1992. Acute traumatic central cord syndrome: MRI-pathological
465 correlations. *Neuroradiology* 34, 85–94. <https://doi.org/10.1007/BF00588148>

466 Schmidt, H., Heuer, F., Simon, U., Kettler, A., Rohlmann, A., Claes, L., Wilke, H.-J., 2006.
467 Application of a new calibration method for a three-dimensional finite element model of
468 a human lumbar annulus fibrosus. *Clin. Biomech.* 21, 337–344.

469 Schneider, R.C., Cherry, G., Pantek, H., 1954. The syndrome of acute central cervical spinal cord
470 injury; with special reference to the mechanisms involved in hyperextension injuries of
471 cervical spine. *J. Neurosurg.* 11, 546–577. <https://doi.org/10.3171/jns.1954.11.6.0546>

472 Schneider, R.C., Thompson, J.M., Bebin, J., 1958. THE SYNDROME OF ACUTE CENTRAL CERVICAL
473 SPINAL CORD INJURY. *J. Neurol. Neurosurg. Psychiatry* 21, 216–227.

474 Shedid, D., Benzel, E.C., 2007. CERVICAL SPONDYLOSIS ANATOMYPATHOPHYSIOLOGY AND
475 BIOMECHANICS. *Neurosurgery* 60, S1-7-S1-13.
476 <https://doi.org/10.1227/01.NEU.0000215430.86569.C4>

477 Shirazi-Adl, A., Ahmed, A., Shrivastava, S., 1986. A finite element study of a lumbar motion
478 segment subjected to pure sagittal plane moments. *J. Biomech.* 19, 331–350.

479 Song, J., Mizuno, J., Inoue, T., Nakagawa, H., 2006. Clinical evaluation of traumatic central cord
480 syndrome: emphasis on clinical significance of prevertebral hyperintensity, cord
481 compression, and intramedullary high-signal intensity on magnetic resonance imaging.
482 *Surg. Neurol.* 65, 117–123. <https://doi.org/10.1016/j.surneu.2005.06.045>

483 Stevenson, C.M., Dargan, D.P., Warnock, J., Sloan, S., Espey, R., Maguire, S., Eames, N., 2016.
484 Traumatic central cord syndrome: neurological and functional outcome at 3 years.
485 *Spinal Cord* 54, 1010–1015. <https://doi.org/10.1038/sc.2016.34>

486 Tani, T., Yamamoto, H., Kimura, J., 1999. Cervical spondylotic myelopathy in elderly people: a
487 high incidence of conduction block at C3–4 or C4–5. *J. Neurol. Neurosurg. Psychiatry* 66,
488 456–464. <https://doi.org/10.1136/jnnp.66.4.456>

489 Taso, M., Fradet, L., Callot, V., Arnoux, P.J., 2015. Anteroposterior compression of the spinal
490 cord leading to cervical myelopathy: a finite element analysis. *Comput. Methods*
491 *Biomech. Biomed. Engin.* 18, 2070–2071.
492 <https://doi.org/10.1080/10255842.2015.1069625>

493 Thompson, C., Mutch, J., Parent, S., Mac-Thiong, J.-M., 2015. The changing demographics of
494 traumatic spinal cord injury: An 11-year study of 831 patients. *J. Spinal Cord Med.* 38,
495 214–223. <https://doi.org/10.1179/2045772314Y.0000000233>

496 Wagnac, E., Arnoux, P.-J., Garo, A., Aubin, C.-E., 2012. Finite element analysis of the influence of
497 loading rate on a model of the full lumbar spine under dynamic loading conditions. *Med.*
498 *Biol. Eng. Comput.* 50, 903–915.

499 Wagnac, E., Arnoux, P.-J., Garo, A., El-Rich, M., Aubin, C.-E., 2011. Calibration of hyperelastic
500 material properties of the human lumbar intervertebral disc under fast dynamic
501 compressive loads. *J. Biomech. Eng.* 133, 101007. <https://doi.org/10.1115/1.4005224>

502 Yu, Y.L., Stevens, J.M., Kendall, B., Boulay, G.H. du, 1983. Cord shape and measurements in
503 cervical spondylotic myelopathy and radiculopathy. *Am. J. Neuroradiol.* 4, 839–842.

504

505

506

507

508 **Appendix 1:** Results from the dynamic calibration of disks: Finite element model material
509 properties

510

511 **Appendix 1a:** Material properties of disk

	Type of elements	Material law	Material parameters (units: g, mm, ms)	References
Disks:				
Annulus	hexahedral Brick	Hyper-elastic Mooney Rivlin	Coef. in Appendix 1b	(Barker, et al., 2014)
Nucleus	hexahedral Brick	Hyper-elastic Mooney Rivlin	Coef. in Appendix 1b	(Barker, et al., 2014)
Collagen fibers	Spring	Force-displacement non-linear curves with scaling factor by region	Scaling factors: Anterior = 1.2 Posterior = 0.85 Lateral = 1.03	(Schmidt et al., 2006) (Shirazi-Adl et al., 1986)

512

513

514

515

516

517

518

519

520

521

522 **Appendix 1b:** Coefficients of the Mooney-Rivlin hyper-elastic material laws of the annulus and
523 nucleus for each spinal functional unit

Spinal unit	C2-C3	C3-C4	C4-C5	C4-C5	C5-C6	C6-C7	C6-C7	C7-T1
Annulus								
Anterior								
C ₁₀	0.72	2.88	0.11	0.36	0.72	0.72	7.20	10.80
C ₀₁	-0.18	-0.72	-0.03	-0.09	-0.18	-0.18	-1.80	-2.70
Lateral								
C ₁₀	0.72	2.88	0.11	0.36	0.72	0.18	10.80	10.80
C ₀₁	-0.18	-0.72	-0.03	-0.09	-0.18	-0.05	-2.70	-2.70
Posterior								
C ₁₀	0.72	5.76	0.45	0.36	5.76	0.07	10.80	5.76
C ₀₁	-0.18	-1.44	-0.11	-0.09	-1.44	-0.02	-2.70	-1.44
Nucleus								
C ₁₀	0.96	7.68	1.92	0.48	0.96	0.96	0.96	14.40
C ₀₁	-0.72	-5.76	-1.44	-0.36	-0.72	-0.72	-0.72	-10.80

524